THE JOURNAL OF PHYSICAL CHEMISTRY C

Article

pubs.acs.org/JPCC

Improved Ductility of Boron Carbide by Microalloying with Boron Suboxide

Bin Tang,[†,‡,§] Qi An,[‡,§] and William A. Goddard III*[,‡]

[†]StateKey Laboratory of Electronic Thin Films and Integrated Devices, University of Electronic Science and Technology ofChina, Chengdu 610054, China

[‡]Materialsand Process Simulation Center, CaliforniaInstitute of Technology, Pasadena, California 91125, United States

ABSTRACT: Boron carbide (B_4C) is the third hardest material in nature, but applications are hindered by its brittle failure under impact. We found that this brittle failure of B_4C arises from amorphous shear band formation due to deconstruction of icosahedral clusters, and on the basis of this model we suggest and validate with quantum mechanics (QM, PBE flavor of density function theory) that a laminated B_4C−B_6O composite structure will eliminate this brittle failure. Using QM to apply shear deformations along various slip systems, we find that the (001)/[100] slip system has the lowest maximum shear strength, indicating it to be the most plausible slip system. We find that this composite structure has a shear strength of 38.33 GPa, essentially the same as that of B_4C (38.97 GPa), indicating the same intrinsic hardness as B_4C. However, the critical failure strain for (001)/[100] slip in the composite is 0.465, which is 41% higher than B_4C, indicating a dramatically improvement on ductility. This arises because incorporation of B_6O prevents the failure mechanism of B_4C in which the carbene formed during shear deformation reacts with the C−B−C chains. This suggests a new strategy for designing ductile superhard ceramics.

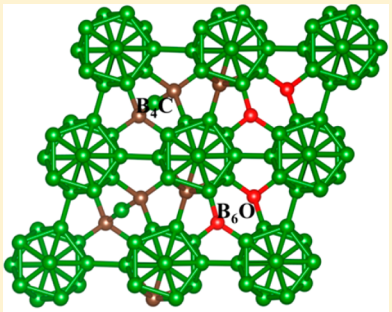

Laminated B_4C with B_6O leads to a composite with increased ductility

1. INTRODUCTION

Because of their extreme high hardness above 40 GPa, superhard materials are widely used in the manufacturing of abrasives, polishing and cutting tools, and wear-resistant coatings.[1−6] Boron-based compounds such as boron carbide (B_4C), boron suboxide (B_6O), and various boron phases (α, β) are the most promising types among these materials.[7,8] In particular because of its high hardness, low density (~2.52 g cm^{-3}), high melting point (~2540 °C), good chemical inertness, high Young's modulus (~445 GPa), and high thermal conductivity (~30 W m^{-1} K^{-1}),[1,8−11] B_4C has been used extensively in advanced contact-mechanical and tribological applications where strength, weight, and conductivity are critical. Although B_4C is a promising lightweight body armor material,[8,12] with a high Hugoniot elastic limit (HEL) of 17−20 GPa that is critical for body armor materials, B_4C displays abnormal brittle failure under hypervelocity impact and high pressures that impedes such engineering applications as structural and functional materials.[8,10,12]

Recent experiments observed the formation of local amorphous bands (1−3 nm wide and 100−200 nm long) under high velocity impact and nanoindentation experiments, which likely underlie the brittle failure.[9,10,12] Indeed, our recent QM studies[13] discovered a unique deformation mechanism responsible for this amorphous shear band formation as crystalline B_4C shears along the $(01\bar{1}1)/\langle\bar{1}101\rangle$ slip system that is consistent with experimental observation.[10] Furthermore, our large-scale (~200 000 atoms/cell) reactive-molecular-dynamics simulations of shear deformations of B_4C found that brittle failure in B_4C arises because fracture of the icosahedra to form amorphous regions increases the local density, leading to tension-induced cavitation, crack formation, and failure.[14] These studies provide the atomistic mechanism underlying the intrinsic brittle failure of B_4C.

Lightweight B_6O has properties similar to those of B_4C, also combining great hardness with low mass density, high thermal conductivity, high chemical inertness, and excellent wear resistance.[15,16] Although nanoindentation experiments observed similar amorphous shear band formation along the $(01\bar{1}1)$ plane in B_6O,[16] our QM shearing studies of single crystal B_6O along the same slip system $(01\bar{1}1)/\langle\bar{1}101\rangle$ show an unusual structural recovery without fracture of icosahedra.[17] We conclude that this difference between the QM study and experiment arises from the difference in loading conditions. In experimental indentation conditions, a component of compressive stress always accompanies the shear components. The deformation mechanism deduced from our QM simulations[17] suggests that incorporating B_6O into B_4C might dramatically improve the ductility of these superhard materials.

Recent experiments synthesizing and consolidating new composite superhard ceramics from single phase boron-containing particles have shown improved performance in applications ranging from high pressure solid synthesis to nonequilibrium spark plasma chemistry.[18−23] For example,

Received: August 19, 2015
Revised: October 5, 2015
Published: October 7, 2015

DOI: 10.1021/acs.jpcc.5b08086
J. Phys. Chem. C 2015, 119, 24649−24656

several multiply composite superhard boron-containing particles have been synthesized including B_6O–B_4C,[19,20,23] B_6O–cBN,[22] and B_4C–TiB_2.[21] As compared to single phase materials, these multiply composite solids lead to much better sinterability and physical properties.[19,23] It has been reported that B_6O–40 vol % c-BN composition with an average grain size of 0.5 mm yields Vickers microhardness values of up to 46 GPa (as compared to 38 GPa for single phase materials).[22] Also, a maximum hardness of 42 GPa was achieved for the 68.6 vol % B_4C–ZrB_2 composition due to grain-boundary strengthening improved by nanosized ZrB_2.[18]

Among these superhard materials, B_6O and B_4C have the same space group and similar lattice parameters; therefore, we speculated that a solid–solution interlayer between B_6O and B_4C crystals could be formed during the sintering reaction that might increase the hardness and toughness properties.[19] For example, the fracture toughness of the nanostructured B_6O–B_4C improves to 8.72 MPa $m^{1/2}$ in contrast to 1.3 MPa $m^{1/2}$ of the single phase B_4C.[8,19] In these systems, the B_6O and B_4C grains were both well-dispersed with respect to each other, suggesting that interlayer bonding is critical to the improved properties.[19,23] To validate such concepts, we used QM to examine how atomistic level bonding structure between these two components might affect the mechanical properties.

In this Article, we investigate a laminated composite structure of B_4C–B_6O in which layers of B_4C alternate with B_6O. This is meant to model 5–10 nm particles, which at our scale would be essentially flat. We then sheared the composite structure along various slip systems both parallel to and perpendicular to the ordered planes to determine which configurations require the least shear stress. We find that the shear strength of the most plausible slip system is very close to the ideal shear strength of B_4C, indicating an intrinsic hardness similar to that of B_4C. More important, the critical failure strain for this slip system is 41% larger than that of perfect B_4C, indicating a dramatically improved toughness. We describe the deformation mechanisms along various slip systems to provide an atomistic understanding of the deformation mechanisms and its coupling to the mechanical properties for these composite ceramics.

2. COMPUTATIONAL DETAILS

All QM simulations were performed used the Vienna Ab Initio Simulation Package (VASP) periodic code with plane wave basis sets.[24–26] We used an energy cutoff of 600 eV in all of the simulations to provide excellent convergence on energy, force, stress, and geometries. We used the projector-augmented wave pseudopotentials for the Perdew–Burke–Ernzerhof (PBE) exchange-correlation density functional.[27] The energy error for convergence of the electronic self-consistent field (SCF) and forces for geometry optimization were set equal to 10^{-6} eV and 10^{-3} eV/Å, respectively. We used the Monkhorst–Pack grid ($4 \times 8 \times 8$) in the k-space for geometry optimization and ($2 \times 2 \times 2$) for shear deformations.

To examine the shear deformation, we imposed the strain for a particular shear plane, while allowing full structure relaxation for the other five strain components.[28] The residual stresses after relaxing the other five strain components in shear deformations were less than 0.5 GPa. To denote the slip directions and planes, this Article uses the three number index rhombohedral representation.

To gain a deeper insight into the nature of the covalent bonding and lone pair formation, we analyzed the electronic structures using the electron localization function (ELF).[29,30] The ELF values range from 0 to 1 with values close to 1 corresponding to the highly localized electrons typical for two-center–two-electron bonds or nonbonding electron lone pairs in molecules.

3. RESULTS AND DISCUSSION

3.1. Geometric Structures. Experimental and QM studies agree that the B_4C crystal structure has rhombohedral symmetry with the $R\bar{3}m$ space group.[1,8,13] The unit cell of B_4C contains one 12-atom icosahedron located at apexes of the primitive cell with one 3-atom linear chain aligned along the $[111]_r$ direction. Each icosahedron involves two types of crystallographic sites: six polar sites (denoted as p) connecting directly to other icosahedra and six equatorial sites (denoted as e) connecting with the 3-atom chains.

The B_4C structure was originally proposed to consist of one B_{12} icosahedron and one C–C–C chain, denoted as $B_{12}(CCC)$.[31] Later, X-ray diffraction (XRD) determined that the chain is C–B–C so that the icosahedron must be $B_{11}C$, but whether the C is at the polar or equatorial site is not determined experimentally.[32] QM calculations predicted that $(B_{11}C_p)(CBC)$ is the ground-state structure, with $(B_{11}C_e)$-(CBC) 0.29 eV/unit cell higher in energy.[13] One can think of this $(B_{11}C_p)(CBC)$ structure as having a B^+ in the C–B–C chain making strong σ bonds to the two C of the linear C–B–C chain, transferring one electron to the icosahedron to provide the 26 skeleton electrons within the icosahedron needed to satisfy Wade's rule.[33] Thus, one can write the structure for B_4C as $(B_{11}C_p)^{1-}(CBC)^{1+}$.

The crystal structure of B_6O is similar to that of B_4C, leading to a rhombohedral lattice with the $R\bar{3}m$ space group. The unit cell is composed of one B_{12} icosahedral cluster at the apexes of the rhombohedral unit cell and one O–O chain along the trigonal axis.[7,16,34] However, each oxygen atom bonds to three icosahedra through B–O single bonds with 1.50 Å bond length, while the distance between two chain oxygen atoms is 3.07 Å, precluding direct O–O bonding.[35] Because each O atom makes 3 σ bonds in a plane, it must have one π-like lone pair, making it a formal O^+. Thus, again the B_{12} icosahedron will gain 2 electrons to provide the 26 skeleton electrons needed to satisfy Wade's rule. This leads to a representation as $(B_{12})^{2-}(O)^+(O)^+$ for B_6O.

To obtain what we consider to be the best interfacial structure of the (B_4C)–(B_6O) composite, we constructed a laminated structure with each B_4C layer alternating with a B_6O layer along the [100] direction, as shown in Figure 1. In this laminated structure, both icosahedral clusters $(B_{12})^{2-}$ and $(B_{11}C_p)^{1-}$ obtain electrons from chain atoms to provide 26 skeletal electrons, satisfying Wade's rule. In addition, both the $(O)(O)^{2+}$ chain and the $(C–B–C)^{1+}$ chain connect to three $(B_{12})^{2-}$ and to three $(B_{11}C_p)^{1-}$. After structure optimization, the QM finds that the linear $(C–B–C)^{1+}$ chains bend to an angle of 173.5° with respect to the $(B_{12})^{2-}$ icosahedra, due to interactions of the C–B–C chains with the adjacent icosahedra. The predicted lattice parameters for the laminated structure are a = 10.37 Å, b = 5.18 Å, c = 5.11 Å, α = 64.47°, β = 64.59°, and γ = 64.12°, leading to a density of 2.56 g/cm^3, which can be compared to densities of 2.52 and 2.65 g/cm^3 for B_4C and B_6O, respectively.

3.2. Shear Deformation and Failure Mechanism. On the basis of previous QM and experimental observations of amorphous shear band formation, we consider that the $(100)_r$ plane is the most plausible slip plane for both B_4C and

DOI: 10.1021/acs.jpcc.5b08086
J. Phys. Chem. C 2015, 119, 24649–24656

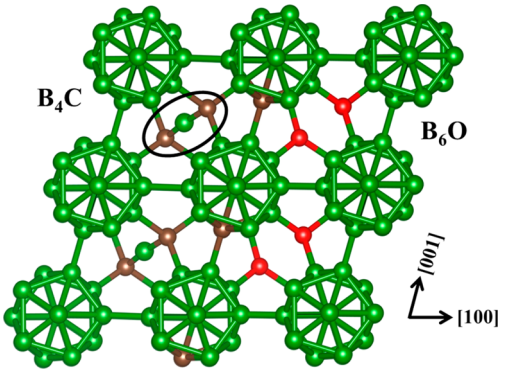

Figure 1. Laminated composite structure of B_4C–B_6O. The left layer is from B_4C with the C–B–C chain along the [111] direction. The right layer is from B_6O structure with the (O)(O) chain along the [111] direction. The C–B–C chain (in oval) bends to 173.5° because of interactions of sides of the $(C–B–C)^{1+}$ chains with the icosahedra. The boron, carbon, and oxygen atoms are represented by the green, sienna, and red balls, respectively. This structure was drawn using the VESTA software.[37]

B_6O.[10,13,16,17] For the QM simulations, we first expanded the laminate structure to a (2 × 2) cell along the [010] and [001] directions. We then considered shearing the system along six different slip systems: (001)/[010], (001)/[100], (100)/[001], (100)/[010], (010)/[001], and (010)/[100], to determine the most favorable slip system. The stress–strain relationships of these six slip systems are displayed in Figure 2. Among these

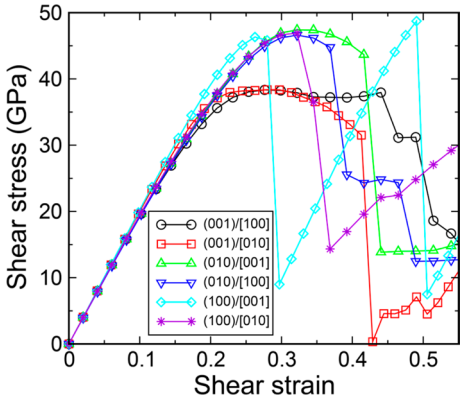

Figure 2. Stress–strain relationship for composite B_4C–B_6O shearing along various slip systems. The (001)/[100] slip (black) has the lowest maximum shear strength of 38.33 GPa, indicating this to be the most plausible activated slip system under high pressure. The (001)/[010] slip (red) has a similar low maximum shear strength of 38.37 GPa, indicating this is also likely activated under high pressure. The presence of two orthogonal favorable slip sytems should aid to increase ductility.

slip systems, we find that (001)/[100] has the lowest maximum shear strength of 38.33 GP, indicating this to be the most plausible slip system. The second most plausible slip system, (001)/[010], leads to a maximum shear strength of 38.37 GPa, which is only slightly higher, indicating this to be a slip system likely to be activated. The critical failure strain for the (001)/[100] slip system is 0.465, while that of the (001)/[010] slip system is 0.429, which are 41% and 30% larger as compared to the perfect B_4C of 0.331,[13] respectively. This indicates a dramatic improvement in the toughness. In addition, the availability of two favorable slip systems should improve ductility (in the same way that a fcc metal is more ductile than hcp).

These results are consistent with the experimental observation that nanostructured B_6O–B_4C composites have a fracture toughness[19] of 8.72 MPa $m^{1/2}$, as compared to 1.3 and 2.2 MPa $m^{1/2}$ for B_4C and B_6O, respectively. Indeed, we find that the composite leads to a stress–strain curve for the (100)/[001] slip system that exhibits a linear increase after failure, indicating a structural recovery similar to that of the perfect B_6O crystal.[17] The predicted maximum shear stress and the critical failure strain are listed in Table 1.

Table 1. Predicted Maximum Shear Stress and Critical Failure Strain for the Laminated Composite B_4C–B_6O Structure Shearing along Various Slip Systems[a]

slip system	ideal shear strength (GPa)	critical failure strain
(001)/[010]	38.37	0.429
(001)/[100]	38.33	0.465
(100)/[001]	46.33	0.297
(100)/[010]	46.91	0.369
(010)/[001]	47.37	0.440
(010)/[100]	46.61	0.392

[a]On the basis of these results, we chose the first two for further study.

To understand the deformation mechanism of the composite structure shearing along (001)/[100], we plotted the structural changes and ELF of these structures in Figures 3 and 4. As the shear strain increases to 0.276 (Figures 3a and 4b) corresponding to the maximum shear stress, the B–C bond stretches from 1.68 Å in the intact structure (Figure 4a) to 2.66 Å. The ELF in Figure 4b shows that after the B–C direct bond between the icosahedra breaks, it leaves a carbene π lone pair on the C atom within the icosahedron. However, in contrast to the perfect B_4C shear deformation where this carbene reacts with the B^+ in the C–B–C chain to deconstruct the icosahedron,[13] the carbene lone pair in the composite structure is close to the O pπ lone pairs with which it cannot react. Thus, the icosahedra remain unfractured as the shear strain increases to 0.44, before the structure starts to fail, as shown in Figure 3b. Finally, as the shear strain increases to 0.489, icosahedron deconstruction initiates, leading to the B_{12} partially disintegrated cluster shown in Figures 3c and 4c. The ELF in Figure 4c shows that the carbene still exists at 0.489 strain, indicating it is not involved in the B_{12} icosahedron deconstruction. Finally, as the shear strain increases to 0.514, the B_{12} icosahedra are fully disintegrated as shown in Figures 3d and 4d. We find that in the composite, it is the B_{12} icosahedron fractures, not the $B_{11}C_p$ icosahedron, indicating that the B_{12} icosahedron is less stable than $B_{11}C_p$.

Because the maximum shear stress for the (001)/[010] slip system is very close to the most plausible slip system, we also examined the failure mechanism for this slip system, as shown in Figure 5. As the shear strain increases to the 0.280 corresponding to the maximum shear stress, the B–B bond between icosahedra increases from 1.71 Å (in the intact structure) to 2.47 Å, so that the B–B bond is broken, as shown in Figure 5a. In addition, the B–C bond between icosahedra increases to 2.95 Å, indicating that it is also broken. As the shear strain increases to 0.413 (before failure), the C–B–C chain interacts with the icosahedra, as shown in Figure 5b. Finally, as the shear strain increases to 0.429, the icosahedra deconstruct because of the interaction of B_{12} with the C–B–C

DOI: 10.1021/acs.jpcc.5b08086
J. Phys. Chem. C 2015, 119, 24649–24656

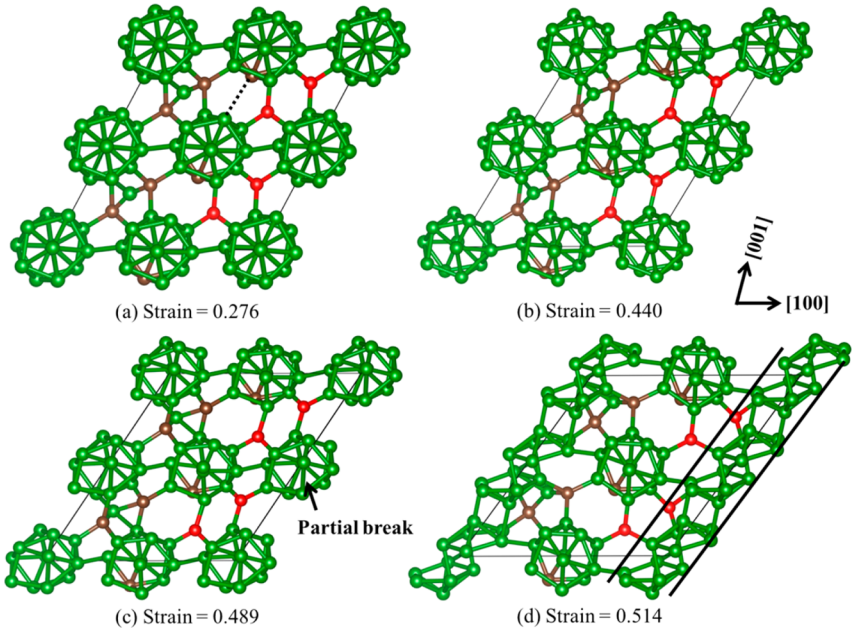

Figure 3. Structural changes during the failure process of composite B_4C–B_6O shearing along the (001)/[100] slip system. (a) The structure at 0.276 strain corresponds to the maximum shear stress. The dashed line indicates the breaking B–C bond. (b) The structure at 0.440 strain, before failure. (c) The structure at 0.489 strain, corresponding to partial failure of icosahedra. (d) The structure at 0.514 strain, corresponding to full deconstruction of icosahedra. The boron, carbon, and oxygen atoms are represented by the green, sienna, and red balls, respectively.

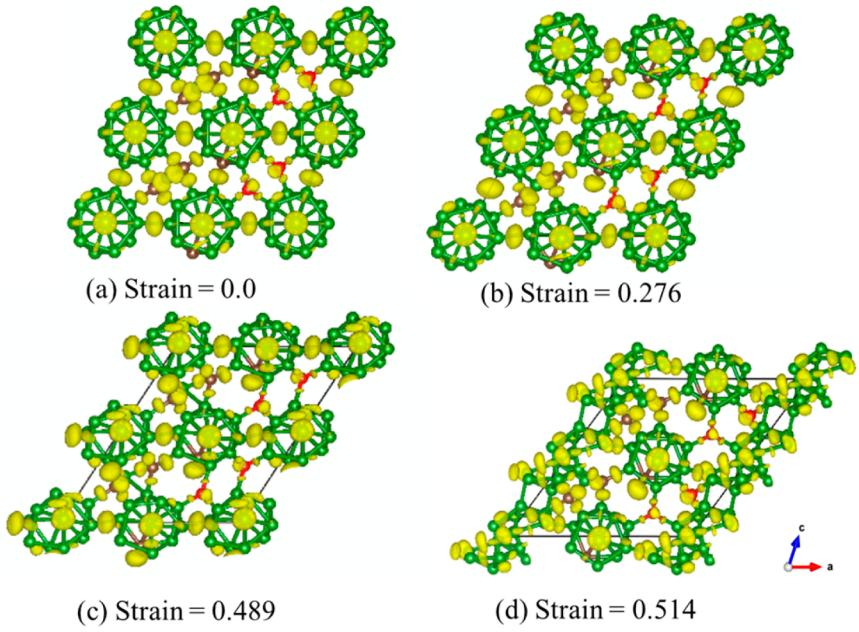

Figure 4. Changes in the electron localization function (value of 0.85) along the pathway to failure of the composite B_4C–B_6O shearing along the (001)/[100] slip system. (a) The intact structure. (b) The structure at 0.276 strain, corresponding to the maximum shear stress. (c) The structure at 0.489 strain, corresponding to partial failure of icosahedra. (d) The structure at 0.514 strain, corresponding to fully deconstructed icosahedra. The boron, carbon, and oxygen atoms are represented by the green, sienna, and red balls, respectively.

chain, as shown in Figure 5c. Not all of the icosahedra deconstruct, as shown in Figure 5d for the rotated structure viewed along the [010] direction.

This deformation mechanism for shear along the (100)/[001] slip system is similar to that for perfect B_6O.[17] The structures before and after structural change are shown in Figure 6. At 0.280 strain (before structural changes), the B–B bond between icosahedra increases to 2.50 Å, indicating that it is breaking, as shown in Figure 6a. As the shear strain increases to 0.297, the structure recovers in the B_6O part without breaking the $B_{11}C_p$ icosahedra, as shown in Figure 6b. This indicates that the composite structure can recover from the strain to reform the stable structure under this particular deformation path.

3.3. Multiple Layer Laminated Structure and Failure Mechanism. To examine how multiple layer structures affect

DOI: 10.1021/acs.jpcc.5b08086
J. Phys. Chem. C 2015, 119, 24649–24656

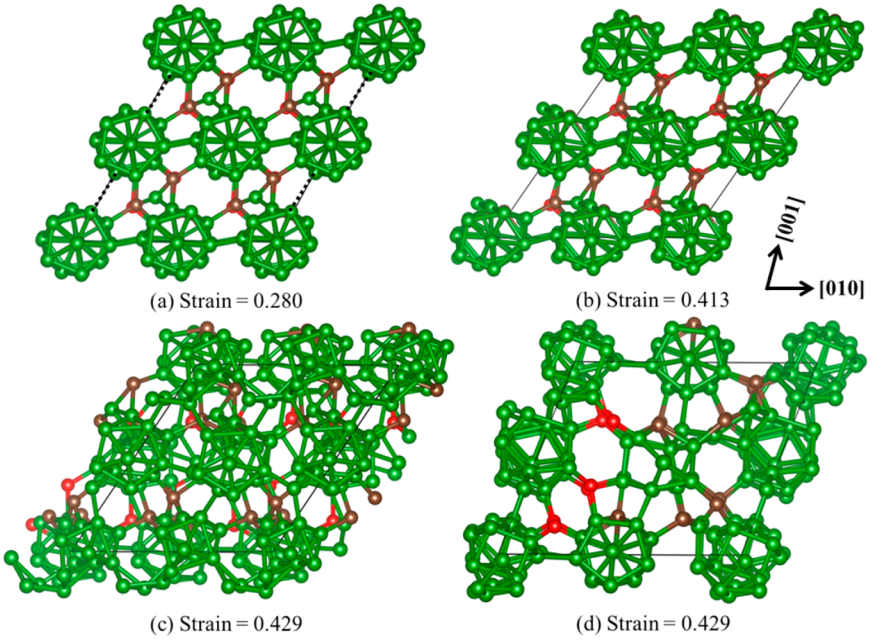

Figure 5. Structural evolution along the failure pathway of the composite B_4C–B_6O shearing along the (001)/[010] slip system. (a) The structure at 0.280 strain, corresponding to the maximum shear stress. The dashed line indicates the breaking B–C bond. (b) The structure at 0.413 strain before failure. (c) The failed structure at 0.429 strain, viewed along the [100] direction. (d) The failed structure at 0.429 strain, viewed along the [010] direction. The boron, carbon, and oxygen atoms are represented by the green, sienna, and red balls, respectively.

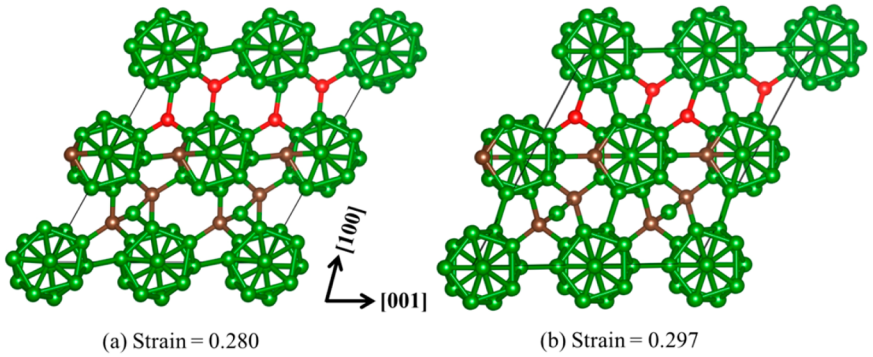

Figure 6. Structural changes before (a) and after (b) the structural recovery for composite B_4C–B_6O shearing along the (100)/[001] slip system. The boron, carbon, and oxygen atoms are represented by the green, sienna, and red balls, respectively.

the deformation mechanism, we constructed a multiple layer model combining 3 layers of B_4C with 2 layers of B_6O and calculated the shear deformation along the most plausible slip system (001)/[100] as shown in Figure 7. The stress–strain relationship shows that the critical failure strain decreases from 0.465 for the one layer structure to 0.429 for the multiple layer structure. This indicates that the multiple layer structure substantially improves ductility, but less than for the one layer structure.

The failure mechanism in Figure 7b,c is similar to the one layer structure. As the strain increases from 0 to 0.254, the B–C bonds between icosahedra break in the B_4C region, as shown in Figure 7b. The C–B–C chain angle bends to 169.3° in the interfacial region (oval in Figure 7c) as the strain increases to 0.416. Yet the C–B–C chain only bends to 172.5° in the interior of B_4C (rectangle in Figure 7c). This indicates that the interior B_4C deforms less than the interfacial region, which arises from the high energy interface accommodating larger strain than the interior region of crystal. This suppresses the interior failure of B_4C until the strain increases to 0.429 as shown in Figure 7d. This enables the multiple layer structure to improve the ductility.

Our simulations showing that the laminate structure leads to improved ductility suggest that a disordered structure with alternating laminates involving various numbers of several B_4C and B_6O layers would have higher ductility than the perfect B_4C. This could lead to a useful B_4C-based glass that retains hardness while improving ductility.

3.4. Biaxial Shear Deformation. Compression plays an indispensable role in the failure behavior under hypervelocity impact. However, shear deformation is the main mechanism for failure in B_4C.[12−14] To consider compression effects in shear deformations while relating them to a realistic physical processes, we calculated the biaxial shear deformation that mimics the indentation conditions for a Vickers indenter and applied this to the laminated structure along the most plausible slip system (001)/[100].[36]

The stress–strain relationship for biaxial shear deformation is displayed in Figure 8a. The laminated structure deforms continuously as the strain increases from 0 to 0.166, where the

DOI: 10.1021/acs.jpcc.5b08086
J. Phys. Chem. C 2015, 119, 24649−24656

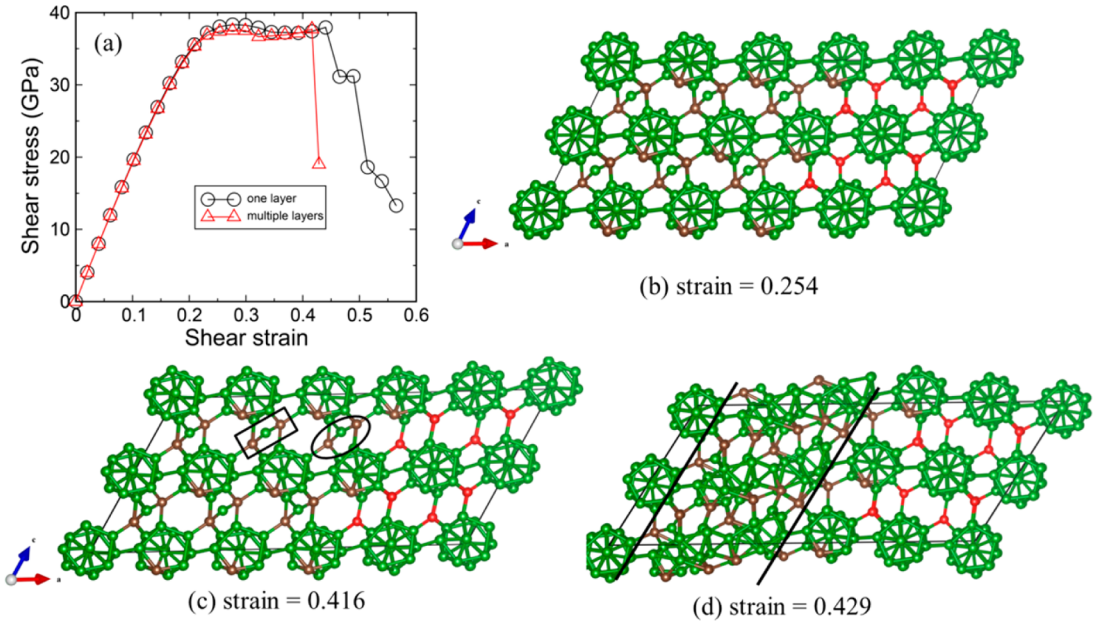

Figure 7. Shear deformation of multiple layer model along the (001)/[100] slip system and compared to the one-layer model. (a) The stress−strain relationship. (b) The structure at 0.254 strain showing the fission of B−C bond between icosahedra. (c) The structure at 0.416 strain showing the larger strain at the B_4C−B_6O interface than that in the interior B_4C. (d) The structure at 0.429 strain showing the failure at B_4C within the solid black line. The boron, carbon, and oxygen atoms are represented by the green, sienna, and red balls, respectively.

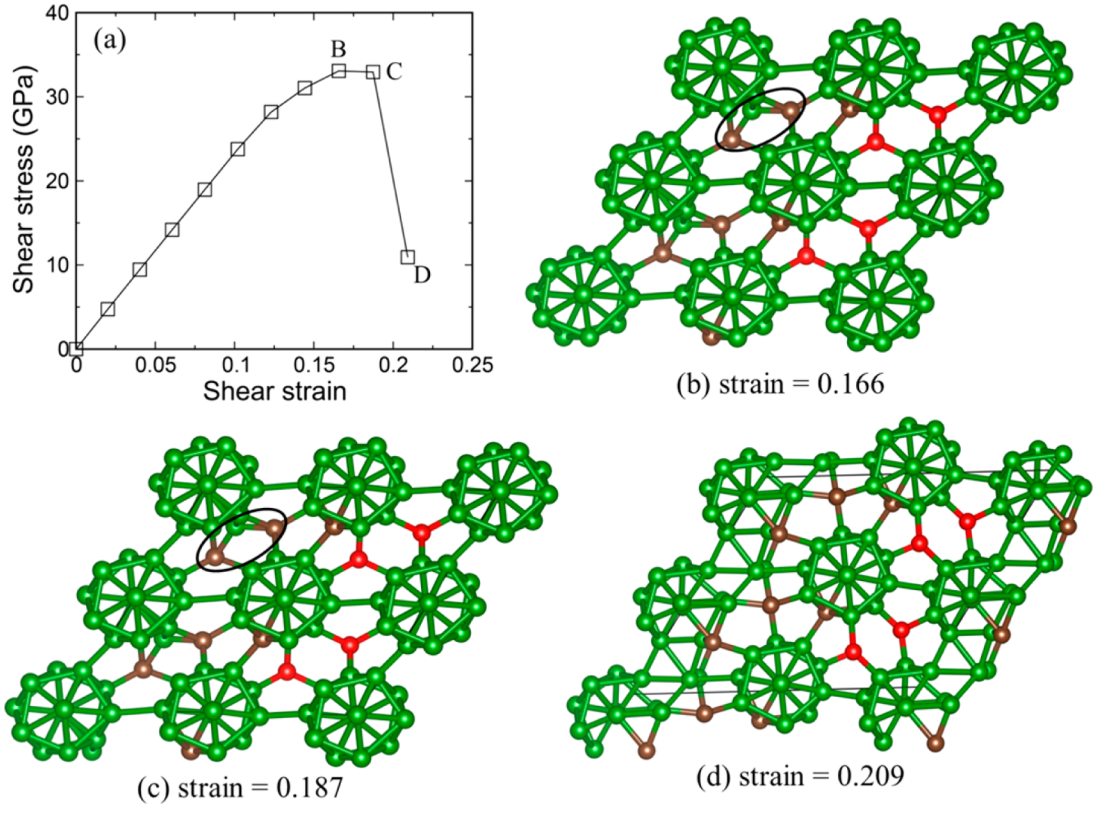

Figure 8. Biaxial shear deformation of laminated structure along (001)/[100] slip system that mimics the indentation conditions. (a) The shear stress−shear strain relationship of biaxial shear deformation. (b) The structure at 0.166 strain corresponding to the maximum shear stress of 33.1 GPa. (c) The structure at 0.187 strain before failure. (d) The failure structure at 0.209 strain. The boron, carbon, and oxygen atoms are represented by the green, sienna, and red balls, respectively.

shear stress reaches its maximum value of 33.1 GPa. The C−B−C chain bends from 173.5° for the unstressed structure to 134.6° because of the highly compressive conditions, as shown in Figure 8b. As the strain increases to 0.187 the C−B−C chain bends to 132.1° (Figure 8c), at which point the failure initiates. Finally, as the strain increases to 0.209, the B_{12} icosahedra layer

DOI: 10.1021/acs.jpcc.5b08086
J. Phys. Chem. C 2015, 119, 24649−24656

disintegrates, as shown in Figure 8d. The biaxial failure mechanism does not involve the B−C bond fission process that occurred for pure shear deformation, indicating that compression can modify the deformation mechanism for experimental impact conditions.

4. SUMMARY

To improve the ductility of B_4C, we use our model for the origin of brittleness to propose a laminated composite structure of B_4C−B_6O. We use QM to examine the shear deformation along various possible slip systems to understand the deformation mechanism for a composite structure. We find that the (001)/[100] slip system requires the smallest maximum shear stress (38.33 GPa), essentially the same as the ideal shear strength (38.97 GPa) of perfect B_4C, indicating a similar intrinsic hardness. However, we find that this composite leads to a critical failure strain that is 41% larger than for perfect B_4C. This is because the presence of B_6O prevents the failure mechanism exhibited by perfect B_4C in which the carbene of a broken cage−cage B−C bond reacts with the C−B−C chain. This indicates that it should be possible to increase the fracture toughness of boron carbide by designing a composite system of B_4C−B_6O, a result consistent with experiments. This may provide useful insight toward the design of other ductile hard ceramics.

AUTHOR INFORMATION

Corresponding Author

*E-mail: wag@wag.caltech.edu.

Author Contributions

§B.T. and Q.A. contributed equally to this work.

Notes

The authors declare no competing financial interest.

ACKNOWLEDGMENTS

This work was supported by the Defense Advanced Research Projects Agency (W31P4Q-13-1-0010), by the U.S. Army Research Laboratory under Cooperative Agreement number W911NF-12-2-0022, and by the National Science Foundation (DMR-1436985).

REFERENCES

(1) Moshtaghioun, B. M.; Cumbrera, F. L.; Ortiz, A. L.; Castillo-Rodriguez, M.; Gomez-Garcia, D. Additive-free Superhard B_4C with Ultrafine-grained Dense Microstructures. *J. Eur. Ceram. Soc.* **2014**, *34*, 841−848.

(2) An, Q.; Goddard, W. A., III; Xiao, H.; Cheng, T. Deformation Induced Solid-solid Phase Transitions in Gamma Boron. *Chem. Mater.* **2014**, *26*, 4289−4298.

(3) Zou, J.; Huang, S.-G.; Vanmeensel, K.; Zhang, G.-J.; Vleugels, J.; Van der Biest, O. Spark Plasma Sintering of Superhard B_4C−ZrB_2 Ceramics by Carbide Boronizing. *J. Am. Ceram. Soc.* **2013**, *96*, 1055−1059.

(4) Jiao, X.; Jin, H.; Liu, F.; Ding, Z.; Yang, B.; Lu, F.; Zhao, X.; Liu, X. Synthesis of Boron Suboxide (B_6O) with Ball Milled Boron Oxide (B_2O_3) under Lower Pressure and Temperature. *J. Solid State Chem.* **2010**, *183*, 1697−1703.

(5) Xiong, M.; Fan, C.; Zhao, Z.; Wang, Q.; He, J.; Yu, D.; Liu, Z.; Xu, B.; Tian, Y. Novel Three-dimensional Boron Nitride Allotropes from Compressed Nanotube Bundles. *J. Mater. Chem. C* **2014**, *2*, 7022−7028.

(6) Leger, J. M.; Haines, J.; Schmidt, M.; Petitet, J. P.; Pereira, A. S.; da Jornada, J. A. H. Discovery of Hardest Known Oxide. *Nature* **1996**, *383*, 401−401.

(7) Hubert, H.; Devouard, B.; Garvie, L. A. J.; O'Keeffe, M.; Buseck, P. R.; Petuskey, W. T.; McMillan, P. F. Icosahedral Packing of B12 Icosahedra in Boron Suboxide (B_6O). *Nature* **1998**, *391*, 376−378.

(8) Domnich, V.; Reynaud, S.; Haber, R. A.; Chhowalla, M. Boron Carbide: Structure, Properties, and Stability under Stress. *J. Am. Ceram. Soc.* **2011**, *94*, 3605−3628.

(9) Subhash, G.; Ghosh, D.; Blaber, J.; Zheng, J. Q.; Halls, V.; Masters, K. Characterization of the 3-D Amorphized zone Beneath a Vickers Indentation in Boron Carbide Using Raman Spectroscopy. *Acta Mater.* **2013**, *61*, 3888−3896.

(10) Reddy, M. K.; Liu, P.; Hirata, A.; Fujita, T.; Chen, M. W. Atomic Structure of Amorphous Shear Bands in Boron Carbide. *Nat. Commun.* **2013**, *4*, 2483.

(11) Shirai, K.; Sakuma, K.; Uemura, N. Theoretical Study of the Structure of Boron Carbide $B_{13}C_2$. *Phys. Rev. B: Condens. Matter Mater. Phys.* **2014**, *90*, 064109.

(12) Chen, M. W.; McCauley, J. W.; Hemker, K. J. Shock-Induced Localized Amorphization in Boron Carbide. *Science* **2003**, *299*, 1563−1566.

(13) An, Q.; Goddard, W. A., III; Cheng, T. Atomistic Explanation of Shear-Induced Amorphous Band Formation in Boron Carbide. *Phys. Rev. Lett.* **2014**, *113*, 095501.

(14) An, Q.; Goddard, W. A., III. Atomistic Origin of Brittle Failure of Boron Carbide from Large Scale Reactive Dynamics Simulations: Suggestions toward Improved Ductility. *Phys. Rev. Lett.* **2015**, *115*, 105501.

(15) He, D. W.; Zhao, Y. S.; Daemen, L.; Qian, J.; Shen, T. D.; Zerda, T. W. Boron Suboxide: As Hard as Cubic Boron Nitride. *Appl. Phys. Lett.* **2002**, *81*, 643−645.

(16) Reddy, M. K.; Hirata, A.; Liu, P.; Fujita, T.; Goto, T.; Chen, M. W. Shear Amorphization of Boron Suboxide. *Scr. Mater.* **2014**, *76*, 9−12.

(17) An, Q.; Goddard, W. A., III. Boron Suboxide and Boron Subphosphide Crystals: Hard Ceramics That Shear without Brittle Failure. *Chem. Mater.* **2015**, *27*, 2855−2860.

(18) Zou, J.; Huang, S.-G.; Vanmeensel, K.; Zhang, G.-J.; Vleugels, J.; Van der Biest, O. Spark Plasma Sintering of Superhard B_4C−ZrB_2 Ceramics by Carbide Boronizing. *J. Am. Ceram. Soc.* **2013**, *96*, 1055−1059.

(19) Chen, C.; He, D.-W.; Kou, Z.; Peng, F.; Yao, L.; Yu, R.; Bi, Y. B_6O-Based Composite to Rival Polycrystalline Cubic Boron Nitride. *Adv. Mater.* **2007**, *19*, 4288−4291.

(20) Solodkyi, I.; Xie, S. S.; Zhao, T.; Borodianska, H.; Sakka, Y.; Vasylkiv, O. Synthesis of B_6O Powder and Spark Plasma Sintering of B_6O and B_6O-B_4C Ceramics. *J. Ceram. Soc. Jpn.* **2013**, *121*, 950−955.

(21) Nikzad, L.; Orrù, R.; Licheri, R.; Cao, G. Fabrication and Formation Mechanism of B_4C−TiB_2 Composite by Reactive Spark Plasma Sintering Using Unmilled and Mechanically Activated Reactants. *J. Am. Ceram. Soc.* **2012**, *95*, 3463−3471.

(22) Itoh, H.; Yamamoto, R.; Iwahara, H. B_6O−c-BN Composites Prepared by High-Pressure Sintering. *J. Am. Ceram. Soc.* **2000**, *83*, 501−506.

(23) Itoh, H.; Maekawa, I.; Iwahara, H. Microstructure and Mechanical Properties of B_6O-B_4C Sintered Composites Prepared under High Pressure. *J. Mater. Sci.* **2000**, *35*, 693−698.

(24) Kresse, G.; Hafner, J. Ab Initio Molecular Dynamics for Liquid Metals. *Phys. Rev. B: Condens. Matter Mater. Phys.* **1993**, *47*, 558−561.

(25) Kresse, G.; Furthmuller, J. Efficiency of Ab-Initio Total Energy Calculations for Metals and Semiconductors Using a Plane-Wave Basis Set. *Comput. Mater. Sci.* **1996**, *6*, 15−50.

(26) Kresse, G.; Furthmüller, J. Efficient Iterative Schemes for Ab Initio Total-Energy Calculations Using a Plane-Wave Basis Set. *Phys. Rev. B: Condens. Matter Mater. Phys.* **1996**, *54*, 11169−11186.

(27) Kresse, G.; Joubert, D. From Ultrasoft Pseudopotentials to the Projector Augmented-Wave Method. *Phys. Rev. B: Condens. Matter Mater. Phys.* **1999**, *59*, 1758−1775.

(28) Roundy, D.; Krenn, C. R.; Cohen, M. L.; Morris, J. W., Jr. Ideal Shear Strengths of fcc Aluminum and Copper. *Phys. Rev. Lett.* **1999**, *82*, 2713−2716.

DOI: 10.1021/acs.jpcc.5b08086
J. Phys. Chem. C 2015, 119, 24649−24656

(29) Becke, A. D.; Edgecombe, K. E. A Simple Measure of Electron Localization in Atomic and Molecular Systems. *J. Chem. Phys.* **1990**, *92*, 5397−5403.
(30) Silvi, B.; Savin, A. Classification of Chemical Bonds Based on Topological Analysis of Electron Localization Functions. *Nature (London, U. K.)* **1994**, *371*, 683−686.
(31) Clark, H. K.; Hoard, J. L. The Crystal Structure of Boron Carbide. *J. Am. Chem. Soc.* **1943**, *65*, 2115−2119.
(32) Morosin, B.; Aselage, T. L.; Feigelson, R. S. Crystal Structure Refinements of Rhombohedral Symmetry Materials Containing Boron-Rich Icosahedra. *MRS Online Proc. Libr.* **1987**, *97*, 145.
(33) Wade, K. The Structural Significance of the Number of Skeletal Bonding Electron-pairs in Carboranes, the Higher Boranes and Borane Anions, and Various Transition-metal Carbonyl Cluster Compounds. *J. Chem. Soc. D* **1971**, *15*, 792−793.
(34) Hubert, H.; Garvie, L. A. J.; Devouard, B.; Buseck, P. R.; Petuskey, W. T.; McMillan, P. F. High-Pressure, High-Temperature Synthesis and Characterization of Boron Suboxide (B_6O). *Chem. Mater.* **1998**, *10*, 1530−1537.
(35) Kobayashi, M.; Higashi, I.; Brodhag, C.; Thevenot, F. Structure of B_6O boron-suboxide by Rietveld refinement. *J. Mater. Sci.* **1993**, *28*, 2129−2134.
(36) Pan, Z.-C.; Sun, H.; Zhang, Y.; Cheng, C.-F. Harder than Diamond: Superior Indentation Strength of Wurtzite BN and Lonsdaleite. *Phys. Rev. Lett.* **2009**, *102*, 055503.
(37) Momma, K.; Izumi, F. VESTA 3 for Three-dimensional Visualization of Crystal, Volumetric and Morphology Data. *J. Appl. Crystallogr.* **2011**, *44*, 1272−1276.

DOI: 10.1021/acs.jpcc.5b08086
J. Phys. Chem. C 2015, 119, 24649−24656